MOF-Based Arginine Nanocarriers for Coordinated Immunometabolic and Antitumor Modulation in Triple Negative Breast Cancer

Amir M. Alsharabasy,[1]* Aibhe Boran,[2] Roberto González-Gómez,[2] Harry Revill,[1] Abhay Pandit,[1] Pau Farràs[1,2]*

[1]CÚRAM, Research Ireland Centre for Medical Devices, University of Galway, Ireland. Postal code: H91 W2TY.

[2]School of Biological and Chemical Sciences, Ryan Institute, University of Galway. Postal code: H91 TK33

*Corresponding Authors: **Amir M. Alsharabasy and Dr**. **Pau Farràs**
CÚRAM, Research Ireland Centre for Medical Devices
University of Galway,
H91 W2TY Galway, Ireland
E-mail: amir.abdo@universityofgalway.ie and pau.farras@universityofgalway.ie

1. Characterization of synthesized MOF nanoparticles

SEM imaging revealed uniform, well-defined polyhedral nanoparticles with submicron dimensions (**Fig. S1A**) suitable for nanoscale delivery. High-magnification SEM images of NH_2-MIL-125 were obtained after suspending the particles in ethanol followed by 3.5 h of ultrasonication prior to deposition onto the sample holder. This process yielded well-dispersed particles with sizes in the range of 300–400 nm **(Fig. S2)**. **Table S1** summarizes the hydrodynamic diameter (HD) and ζ-potential in phosphate-buffered saline (PBS) and PBS + 10% FBS. Upon thermal activation, the particle size increased from 499 nm to 642 nm in PBS ($p < 0.05$) and from 540 nm to 725 nm in PBS + FBS, attributed to mild aggregation following solvent removal.[1] Concomitantly, the ζ-potential decreased from 24.3 ± 2.3 mV to –19.1 ± 1.1 mV, consistent with surface restructuring. The addition of 10% FBS further reduced the ζ-potential to –11 mV, reflecting protein corona formation that masks surface charges.[2,3]

EDX spectra confirmed the expected Ti, O, and C composition of NH_2-MIL-125 (**Fig. S1C and S1E**), while minor Au and Si signals originated from the SEM coating and substrate. Titanium was the predominant element (37.9 wt. %), consistent with the theoretical stoichiometry. FTIR analysis verified framework formation, showing asymmetric/symmetric carboxylate stretches ($\nu_{as}(COO^-) \approx 1540$ cm^{-1}, $\nu_{sym}(COO^-) \approx 1390$ cm^{-1} (**Fig. S3A**), typical of Ti-coordinated ligands.[4] Bands near 1622 cm^{-1} (N–H) and 1420 cm^{-1} (C–N) confirm the presence of the amino-linker, and peaks at 400–800 cm^{-1} correspond to Ti–O vibrations.[5] Solvent-related bands at 1655 cm^{-1} (DMF) diminished after activation,[6,7] confirming guest removal and structural stability.

SEM of MOF-808 revealed spherical, densely packed nanoparticles (< 500 nm; **Fig. S1B**), while EDX confirmed the presence of zirconium (39.99 wt%), oxygen (29.66 wt%), carbon (18.06 wt%), and nitrogen (3.36 wt%) (**Fig. S1D, S1F**). Collectively, these data confirm the successful synthesis of highly crystalline, morphologically uniform NH_2-MIL-125 and MOF-808 nanoparticles with compositions matching their theoretical frameworks, validating their suitability as carriers for Arg.

Both frameworks were thermally activated before loading of L-Arg.This induced notable aggregation of MOF-808 nanoparticles, as reflected by an increase in the HD from 221 nm (pre-activated) to 401 nm in PBS ($p < 0.05$) (**Table S1**). A similar trend was observed in PBS containing 10% FBS, where the particle size increased from 189 nm to 313 nm after activation. This behaviour is likely due to enhanced surface hydrophobicity and stronger interparticle interactions following the removal of residual solvents and modulator species during activation. Concomitantly, the ζ-potential became slightly less negative, shifting from –22.9 ± 0.8 mV to –20.1 ± 1.1 mV in PBS, possibly due to the loss or rearrangement of formate

modulators from Zr_6 nodes. Overall, the ζ-potential values for all MOF-808 formulations remained within –10 to –25 mV, a range consistent with marginal colloidal stability.[8]

Interestingly, unlike NH_2-MIL-125, the dispersion of bare MOF-808 nanoparticles improved in the presence of 10% FBS, with the average size decreasing from 221 nm in PBS to 189 nm in PBS + FBS. This contrasting behaviour may stem from the intrinsic differences in the particle size and aggregation tendencies. Upon exposure to serum, MIL-125 particles, initially characterised by larger size and greater aggregation, likely developed thicker protein coronas, resulting in an apparent increase in size. In contrast, smaller and more monodisperse MOF-808 particles were stabilized by serum proteins, which provided steric repulsion and minimized aggregation. Adsorbed protein layers can enhance colloidal stability even when the ζ-potential approaches neutrality by physically preventing interparticle contact.[2,9] This phenomenon likely accounts for the improved stability of MOF-808 in FBS-containing media.

Comparable stabilization effects were previously reported for NH_2-MIL-125 nanoparticles (230 nm), which maintained a nearly constant size (210–240 nm) after 24 h of incubation in 10% FBS due to protein corona formation.[3] However, such stabilisation was not observed in the MIL-125 samples in this study, likely because their initial size was already significantly larger prior to serum exposure. For all MOF-808 samples, exposure to 10% FBS consistently reduced ζ-potential values to approximately –10 mV, confirming surface charge shielding by the adsorbed proteins. The FTIR spectrum verified the successful formation of the MOF-808 framework. The pristine material exhibited characteristic carboxylate bands at 1617 and 1383 cm^{-1} (**Fig. S3B**), attributed to trimesate linkers and formate modulators capping the Zr_6 nodes, respectively.[10,11] Additional peaks at 1563 and 1443 cm^{-1} correspond to coordinated formate species.[12] Upon activation, these formate-associated features diminished, yielding sharper carboxylate bands (1621 and 1383 cm^{-1}) representative of trimesate linkers.[11] The persistence of the characteristic Zr–O–Zr vibration at 650 cm^{-1} confirmed the retention of the inorganic node and successful generation of open Zr sites.

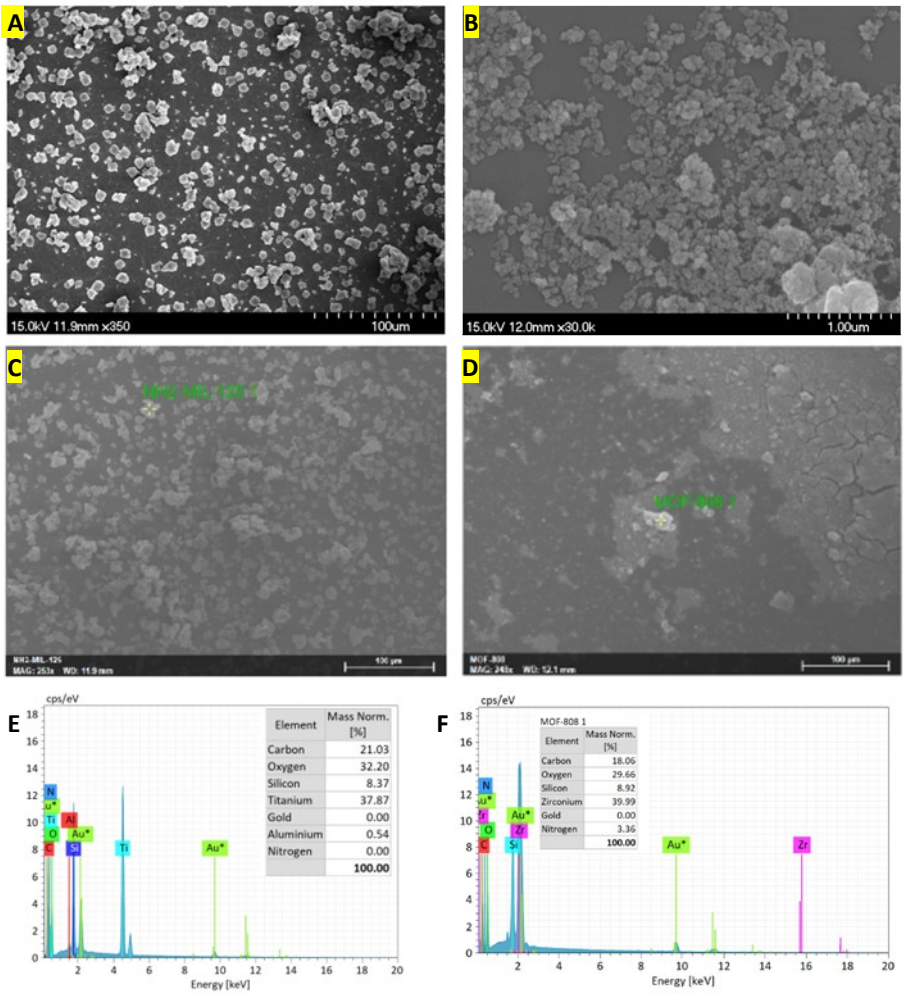

Fig. S1. Structural, morphological, and elemental characterizations of NH_2-MIL-125 and MOF-808 nanoparticles. (a,b) PXRD patterns; (c,e) SEM images and (g) EDX analysis of NH_2-MIL-125; (d,f) SEM images and (h) EDX analysis of MOF-808.

Table S1. Hydrodynamic diameter (HD) and zeta potential (ζ) of NH_2-MIL-125 and MOF-808 nanoparticles before and after activation and loading with L-Arg, measured in PBS and PBS + 10% FBS (mean ± SD, N = 5). “Pre-activation” = as-synthesized; “Activated” = after heat activation; “Arg-loaded” = following L-Arg adsorption;. *a* = significant difference between formulations in PBS + FBS and PBS; *b* = between activated and pre-activated in the same medium; *c* = between Arg-loaded and unloaded under identical conditions;; blank = no significant difference.

Sample	**HD in PBS (nm)**	**HD in PBS+FBS (nm)**	**ζ in PBS (mV)**	**ζ in PBS+FBS (mV)**
NH_2-MIL-125				
Pre-activated	498.7 ± 6.7	539.9 ± 44.1	-24.3 ± 2.3	-11.4 ± 0.2[a]

Arg-loaded-Pre-activated	507.4 ± 18.0	503.1 ± 29.4	-15.0 ± 0.8	-11.8 ± 0.5
Activated	641.7 ± 20.5[b]	725.1 ± 59.1[b]	-19.1 ± 1.5[b]	-10.2 ± 0.6 [a,b]
Arg-loaded Activated	811.5 ± 81.7	483.2 ± 11.9[c]	-15 ± 0.5[c]	-11.9 ± 0.3 [c]
MOF-808				
Pre-activated	221.0 ± 5.1	189.4 ± 6.6[a]	-22.9 ± 0.8	-10.3 ± 0.4[a]
Arg-loaded-Pre-activated	295.1 ± 13.6[c]	241.4 ± 15.6[c]	-22.2 ± 0.9	–10.0 ± 0.4[a]
Activated	400.6 ± 4.7	312.6 ± 29.8[b]	-20.1 ± 1.1[b]	-12.3 ± 0.1[a,b]
Arg-loaded Activated	262 ± 3.7[c]	225.3 ± 10.2[c]	-14.4 ± 0.5	-11.1 ± 0.1

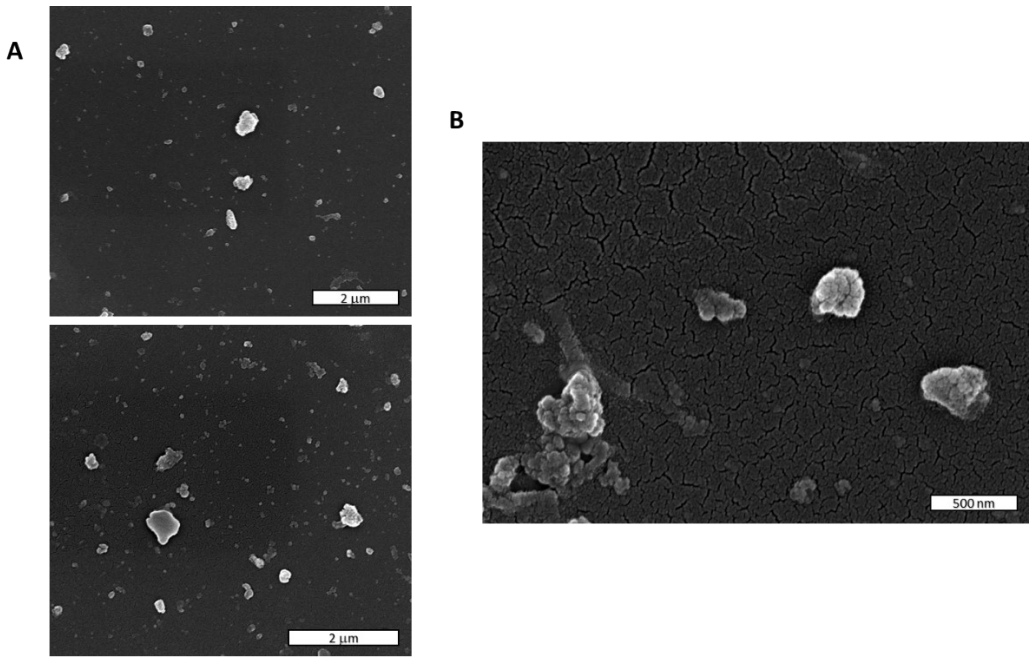

Fig. S2. SEM images of NH2-MIL-125 after 3.5 h sonication in ethanol; **(A)** lower magnification; **(B)** higher magnification.

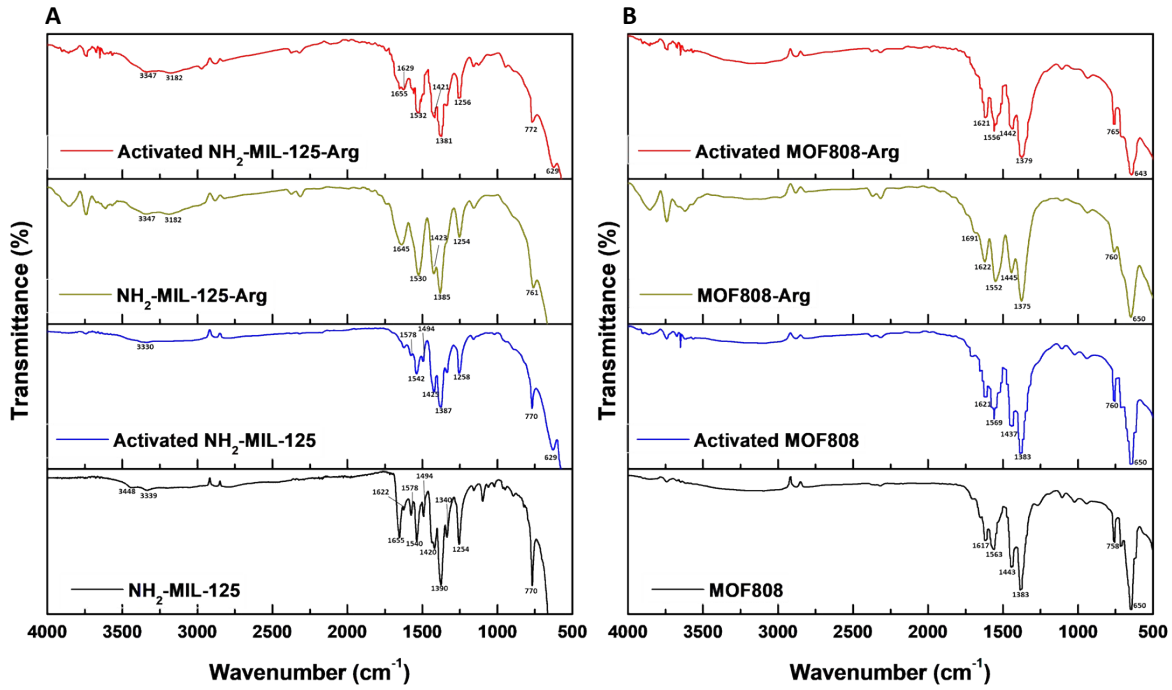

Fig. S3. FTIR spectra. a) NH_2-MIL-125 before and after activation and loading with arginine(Arg). b) MOF-808 before and after activation and loading with Arg.

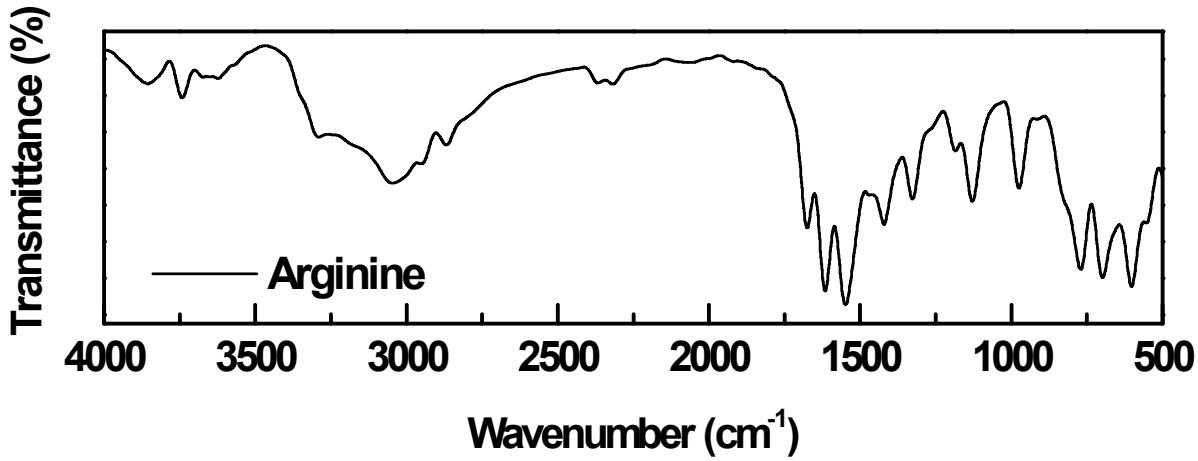

Fig. S4. FTIR spectrum of arginine.

2. Arginine loading and surface modification

L-Arg loading was performed at pH 5.5 to maximise electrostatic attraction between the cationic amino acid and the negatively charged MOF surfaces, while preserving the structural integrity of both NH_2-MIL-125(Ti) and MOF-808. Under these mildly acidic conditions, L-Arg remains positively charged, promoting strong interactions with anionic framework sites without inducing hydrolysis of the Ti–O or Zr–O coordination bonds. The loading efficiency was

determined by quantifying unbound L-Arg in the supernatant and subsequent washing fractions using a ninhydrin-based colorimetric assay.

Changes in surface charge following L-Arg loading provided initial qualitative evidence of adsorption. In PBS, the ζ-potential of NH_2-MIL-125 shifted from −24.3 to −15.0 mV, while activated MOF-808 exhibited a shift from −20.1 to −14.4 mV (**Table S1**), consistent with partial neutralisation of the negatively charged surfaces by the cationic amino acid. The magnitude of these shifts exceeded those reported for small cationic drugs such as pralidoxime (2-PAM),[3] suggesting relatively strong Arg–MOF interactions involving both surface-exposed and pore-lining functional groups.

For NH_2-MIL-125, Arg loading influenced colloidal behaviour in an activation- and medium-dependent manner. In the pre-activated state, Arg incorporation had minimal impact on particle size (507.4 ± 18.0 nm vs. 498.7 ± 6.7 nm), indicating limited aggregation (**Table S1**). In contrast, following activation, Arg loading significantly increased the HD (811.5 ± 81.7 nm vs. 641.7 ± 20.5 nm; $p < 0.05$), suggesting Arg-mediated interparticle bridging through electrostatic and hydrogen-bond interactions with Ti^{4+} centres. Interestingly, this trend was reversed in PBS + 10% FBS, where Arg-loaded activated NH_2-MIL-125 exhibited a smaller HD (483 nm) than the unloaded control (725 nm), indicating that Arg pre-adsorption modulated protein corona formation and reduced serum-induced aggregation.

Successful incorporation of L-Arg into NH_2-MIL-125 was confirmed by FTIR spectroscopy. A distinct band at 1655 cm^{-1}, absent in the unloaded framework, was assigned to the C=N stretching vibration of the guanidinium group (**Fig. S3A**), accompanied by broadening and increased intensity of the N–H stretching region (3000–3500 cm^{-1}).[13] Subtle shifts in the carboxylate stretching region (e.g., ($\nu_{as}(COO^-)$ at 1580–1610 cm^{-1} and $\nu_{sym}(COO^-)$ at 1390–1400 cm^{-1})) further supported the formation of new arginine-associated environments without perturbation of the characteristic Ti–carboxylate vibrations, confirming post-synthetic modification without framework degradation.[2,14] The FTIR spectrum of pure L-Arg is shown in **Fig. S3** for comparison. SEM images revealed uniformly dispersed polyhedral particles with an average size of 10 µm, exhibiting no discernible morphological changes following solvent and thermal activation or subsequent L-Arg loading (**Fig. S5A**).

SEM–EDX analysis further supported successful arginine incorporation, showing a pronounced decrease in Ti content (from 37.9 to 18.8 wt%) accompanied by a concomitant increase in carbon content (to 22.3 wt%) (**Fig. S5A–C**). These compositional changes are consistent with the adsorption of an organic amino acid and suggest effective interaction of L-Arg with surface-exposed and near-surface Ti^{4+} sites through electrostatic and hydrogen-bonding interactions. Elemental mapping revealed a homogeneous spatial distribution of carbon, ox

ygen, and nitrogen that closely colocalised with titanium, indicating uniform L-Arg coordination across the particle surface rather than localized deposition or aggregate formation. Collectively, these findings confirm that L-Arg was successfully adsorbed onto the NH_2-MIL-125 framework through electrostatic and hydrogen-bonding interactions while maintaining the crystalline integrity and morphology of the host structure.

The XRD pattern of NH_2-MIL-125(Ti) displayed sharp reflections consistent with the reported structure of MIL-125(Ti),[15] confirming its high crystallinity and phase purity (**Fig. S5D**). Reflections between 2θ = 5° and 15° correspond to the periodic Ti–O–linker arrangement, indicating the successful incorporation of 2-aminoterephthalic acid. Following L-Arg loading, the overall diffraction pattern is well preserved, with only small shifts indicating a small change in unit cell measurements. This indicates that the crystalline framework and long-range order of NH_2-MIL-125(Ti) remain intact after the loading process. Notably, a moderate reduction in the relative intensity of low-angle reflections was observed following L-Arg loading, which has been widely attributed to partial pore filling and reduced scattering contrast arising from guest inclusion rather than loss of framework crystallinity.[16,17] The absence of additional diffraction peaks associated with crystalline L-Arg further suggests that the amino acid is confined within the MOF pores or present in a non-crystalline form.[18]

This confirms that L-Arg loading does not induce framework collapse or phase transformation and instead occurs through non-destructive coordination or pore-level interactions with the Ti-oxo clusters and/or organic linkers., The ICP-OES analysis revealed marked differences in titanium release kinetics between bare and Arg-loaded NH_2-MIL-125. Sampling-corrected cumulative release calculations showed minimal Ti leaching at early timepoints (≤10 h) for both materials; however, bare NH_2-MIL-125 exhibited a pronounced Ti burst at 36 h, corresponding to a cumulative release of 29 µg Ti (equivalent to 96 µg/mg MOF) (**Fig. S5E**). In contrast, Arg-loaded NH_2-MIL-125 displayed substantially suppressed Ti release over the entire incubation period, reaching only 4.1 µg Ti at 36 h (13.7 µg/mg MOF). These results indicate that L-Arg loading significantly stabilizes the Ti-oxo framework against hydrolytic degradation, an effect that is not detectable by XRD alone but becomes evident through solution-phase metal release analysis.

In contrast to NH_2-MIL-125, L-Arg loading in MOF-808 particles displayed the opposite colloidal trend. In the pre-activated state, Arg loading increased the hydrodynamic diameter (221.0 to 295.1 ± 13.6 nm; $p < 0.05$) (**Table 1**), likely due to bridging flocculation mediated by residual modulator species. Upon activation, however, Arg markedly stabilised the framework, reducing particle size from 400.6 ± 4.7 to 262.0 ± 3.7 nm ($p < 0.05$), consistent with coordination of Arg to exposed Zr^{4+} sites and suppression of aggregation through charge

repulsion and steric stabilisation. Similar stabilising effects were observed in PBS + 10% FBS, suggesting cooperative interactions between L-Arg adsorption and protein corona formation.

FTIR spectra of Arg-loaded MOF-808 exhibited broadened N–H/O–H stretching bands (3000–3600 cm^{-1}) and the emergence of a guanidinium C=N vibration at 1691 cm^{-1}, confirming Arg incorporation (**Fig. S3B**).[13,14] Although overlapping vibrational features preclude the precise assignment of the coordination mode, the persistence of the framework carboxylate stretches and Zr–O–Zr vibration confirms the retention of the structural integrity of MOF-808 after Arg loading.

SEM–EDX analysis corroborated the morphological stability of the Arg-loaded MOF-808. SEM images demonstrated aggregated porous nanoparticles (100–200 nm) forming micrometric clusters, akin to the morphology observed in the unloaded material (**Fig. S6A**). EDX spectra confirmed the presence of Zr, C, O, and N, which is consistent with the expected elemental composition. However, the relative atomic ratio of Zr (19.7 wt%) to C (11.3 wt%) showed a less pronounced change than that observed for NH_2-MIL-125 (**Fig. S6B,C**), suggesting a comparatively lower overall Arg uptake. The XRD pattern of MOF-808 exhibited broad reflections at 2θ = 4–10°, characteristic of its nanocrystalline zirconium-based structure (**Fig. S6D**). These broad diffraction signatures were preserved following L-Arg loading, suggesting that the loading does not induce framework collapse or long-range structural reorganization, and that any Arg–framework interactions occur locally at the Zr_6-oxo clusters or through coordination to accessible sites without disrupting overall structural order.

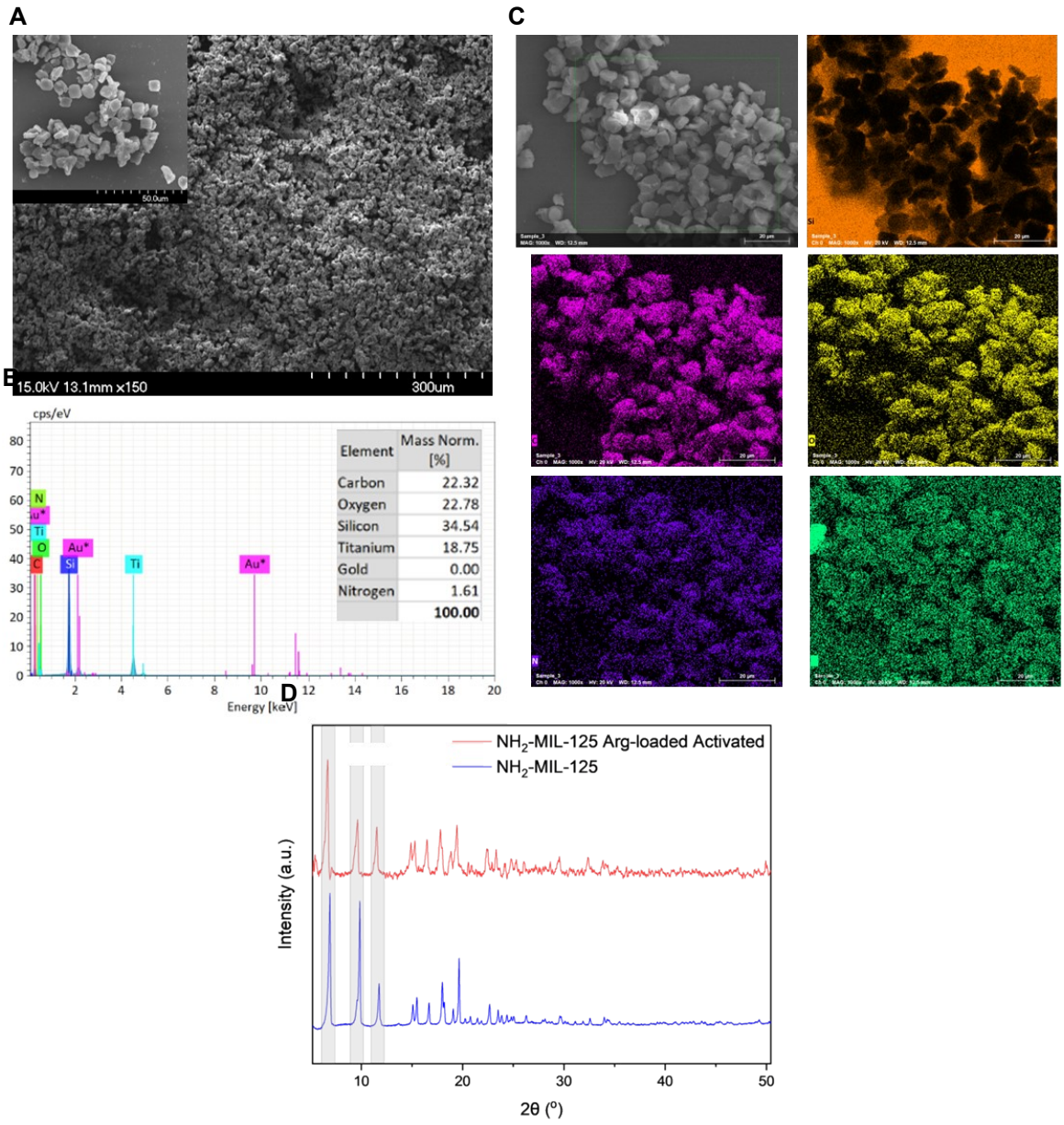

Fig. S5. Structural, morphological and elemental characterization of L-Arg-loaded activated NH_2-MIL-125 nanoparticles. (A) SEM image; (B) EDX spectra and elemental composition; (C) Elemental mapping; (D) PXRD patterns.

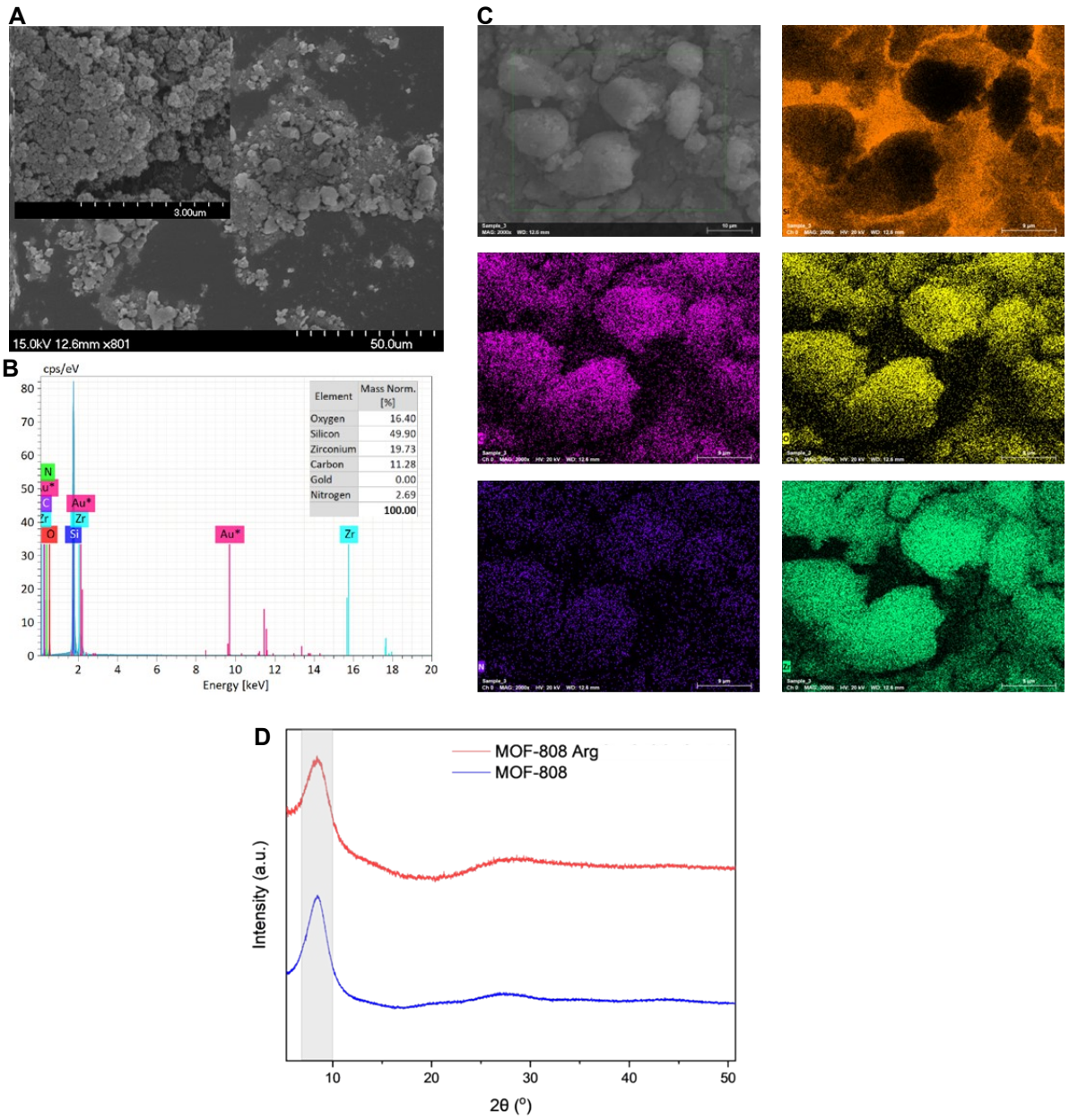

Fig. S6. Structural, morphological and elemental characterization of L-Arg-loaded activated MOF-808 nanoparticles. (A) SEM image; (B) EDX spectra and elemental composition; (C) Elemental mapping; (D) PXRD patterns.

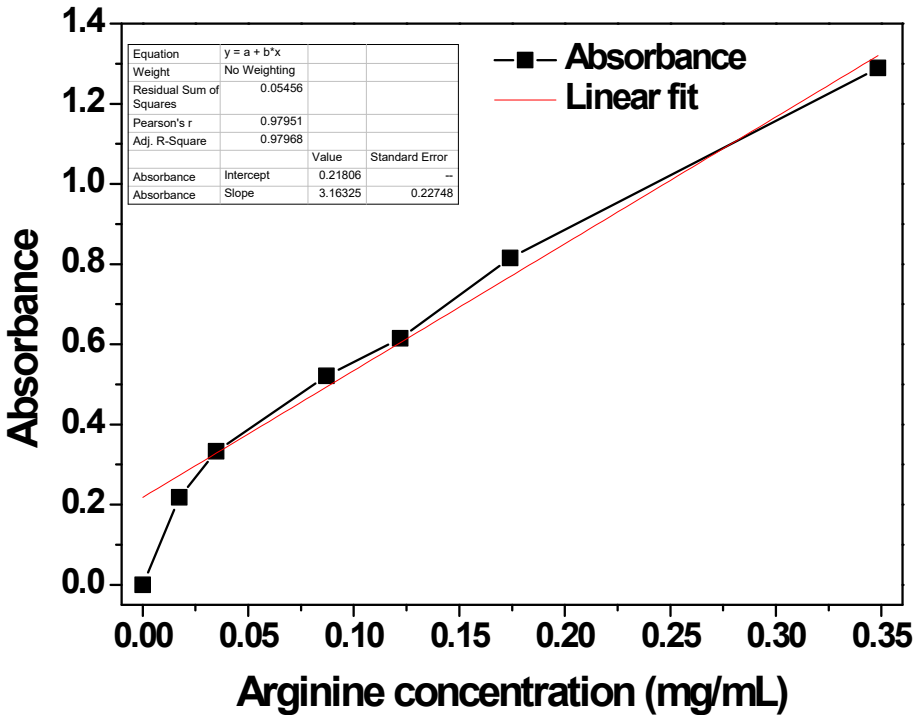

Fig. S7. Standard calibration curve for L-arginine quantification by ninhydrin assay in water.

3. Dose-dependent effects of soluble L-Arg on T-cell mitochondrial metabolism

This study evaluated the direct effect of soluble L-Arg on mitochondrial metabolism in activated human T cells to establish a metabolic benchmark for subsequent arginine-releasing biomaterial studies. Seahorse XF analysis demonstrated a pronounced, dose-dependent modulation of oxidative metabolism following 72 h exposure to L-arginine **(Fig. S8)**. Compared to untreated controls, basal oxygen consumption rate (OCR) was markedly elevated upon L-Arg supplementation, increasing from 103 to 342 pmol/min and 405 pmol/min in cells treated with 500 µM and 2000 µM L-Arg, respectively **(Fig. S8B)**. Maximal respiratory capacity followed a similar trend, reaching 325 pmol/min at 500 µM L-Arg compared to 112 pmol/min in untreated cells, while a lower maximal OCR was observed at 2000 µM (282 pmol/min) **(Fig. S8E)**, suggesting partial limitation of mitochondrial reserve at supraphysiological arginine levels.

ATP-linked respiration was strongly enhanced at 500 µM L-Arg (211 pmol/min), representing an approximately three-fold increase relative to untreated controls (73 pmol/min) **(Fig. S8C)**. In contrast, ATP-linked OCR declined at 2000 µM (124 pmol/min) despite elevated basal respiration, indicating reduced coupling efficiency between electron transport and ATP synthesis. This effect coincided with a substantial increase in proton leak, which rose from 30 pmol/min in untreated cells to 131 pmol/min at 500 µM and further to 280 pmol/min at 2000 µM L-Arg **(Fig. S8D)**. Consistent with these findings, spare respiratory capacity was modestly positive in untreated T cells (9 pmol/min) but became negative following L-Arg exposure,

particularly at 2000 μM (123 pmol/min) **(Fig. S8F)**, indicating exhaustion of mitochondrial reserve capacity under high arginine conditions. Non-mitochondrial oxygen consumption was also elevated in L-Arg-treated cells, increasing from 10 pmol/min in controls to 52 pmol/min at 500 μM and 26 pmol/min at 2000 μM L-Arg **(Fig. S8G)**. Collectively, these data demonstrate that moderate L-Arg supplementation enhances mitochondrial oxidative phosphorylation and ATP production in activated T cells, whereas excessive arginine availability induces mitochondrial uncoupling, increased proton leak, and loss of respiratory reserve. This defines a concentration-dependent metabolic window in which arginine supports immunometabolic fitness, providing a critical reference framework for interpreting the metabolic impact of Arg-releasing biomaterial platforms.

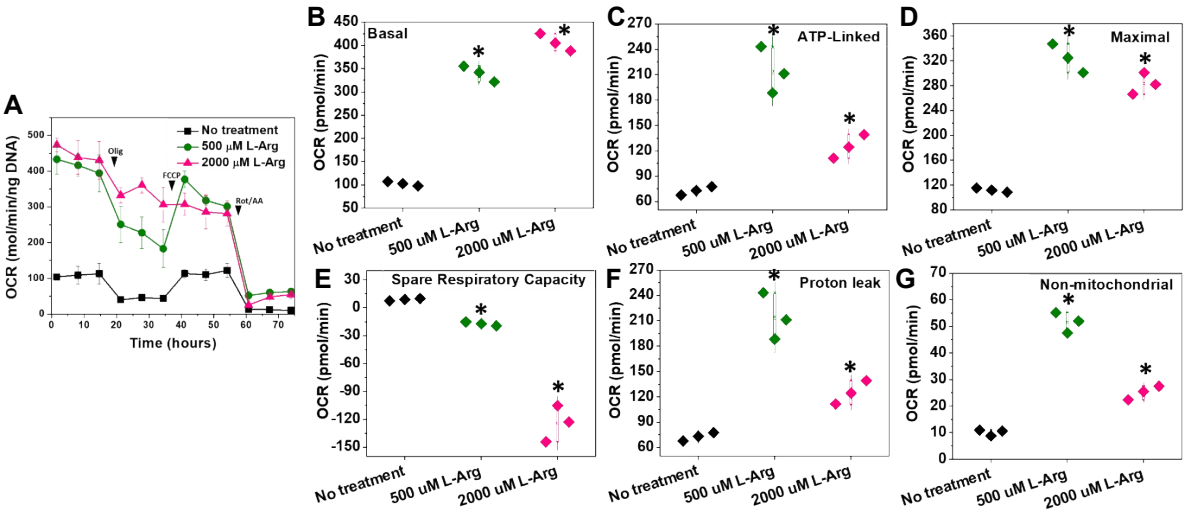

Fig. S8. L-Arginine enhances mitochondrial metabolism in activated human T cells. **(A)** Real-time oxygen consumption rate (OCR) profiles of T cells treated with 500 μM and 2000 μM L-Arg. **(B–G)** Quantification of metabolic parameters including basal respiration, ATP production, proton leak, maximal respiration, spare respiratory capacity, and non-mitochondrial respiration. Data are shown for three independent biological donors (n = 3). Each plotted point represents one donor with three technical replicates. Statistical significance was determined using a two-tailed unpaired t-test: *p < 0.05 versus untreated control.

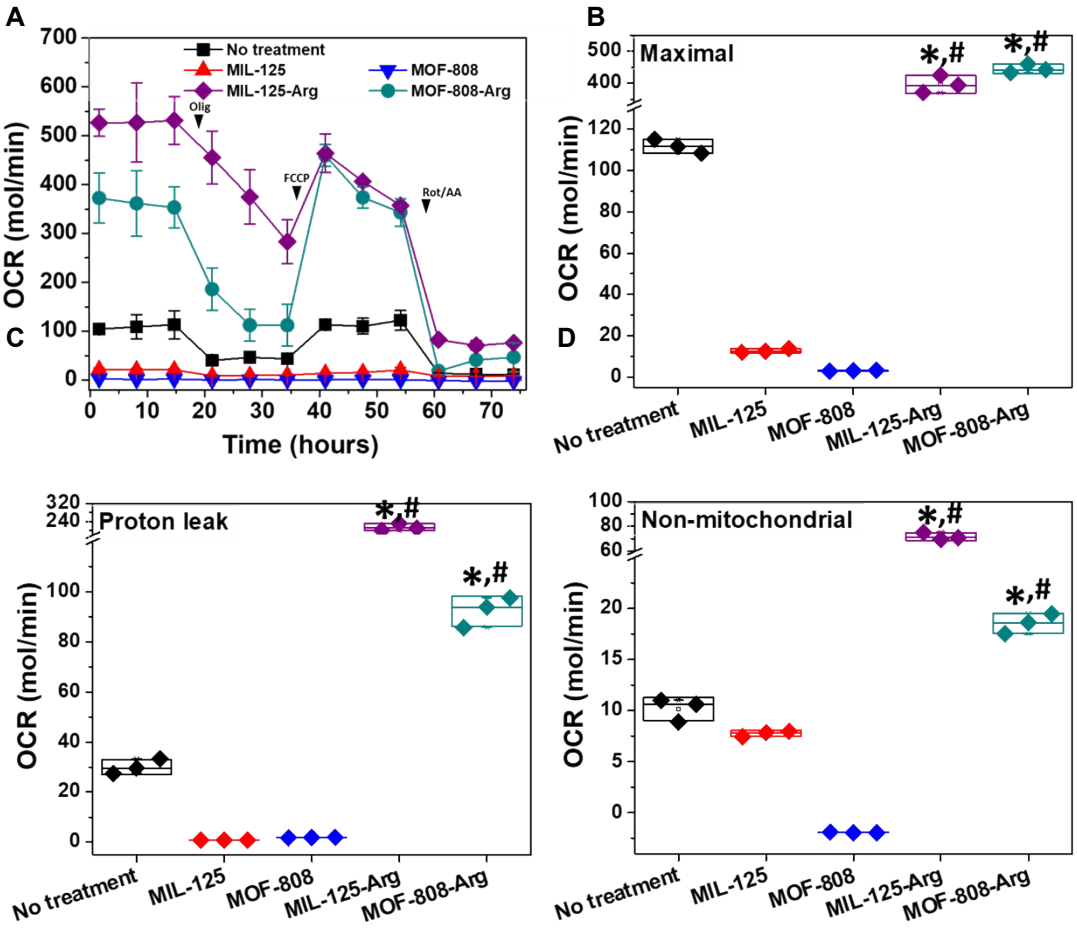

Fig. S9. Arg-loaded MOFs differentially modulate mitochondrial respiration in activated human T cells. **(A)** Real-time oxygen consumption rate (OCR) profiles of T cells treated with 50 μg/mL of unloaded and Arg-loaded NH_2-MIL-125 and MOF-808 nanoparticles. **(B-D)** Quantification of metabolic parameters, including maximal, proton leak, and non-mitochondrial respiration. Data are shown for three independent biological donors (n = 3). Each plotted point represents one donor with three technical replicates. Statistical analysis was performed using the Friedman test for repeated measures, with paired comparisons to untreated control shown as exploratory analyses.

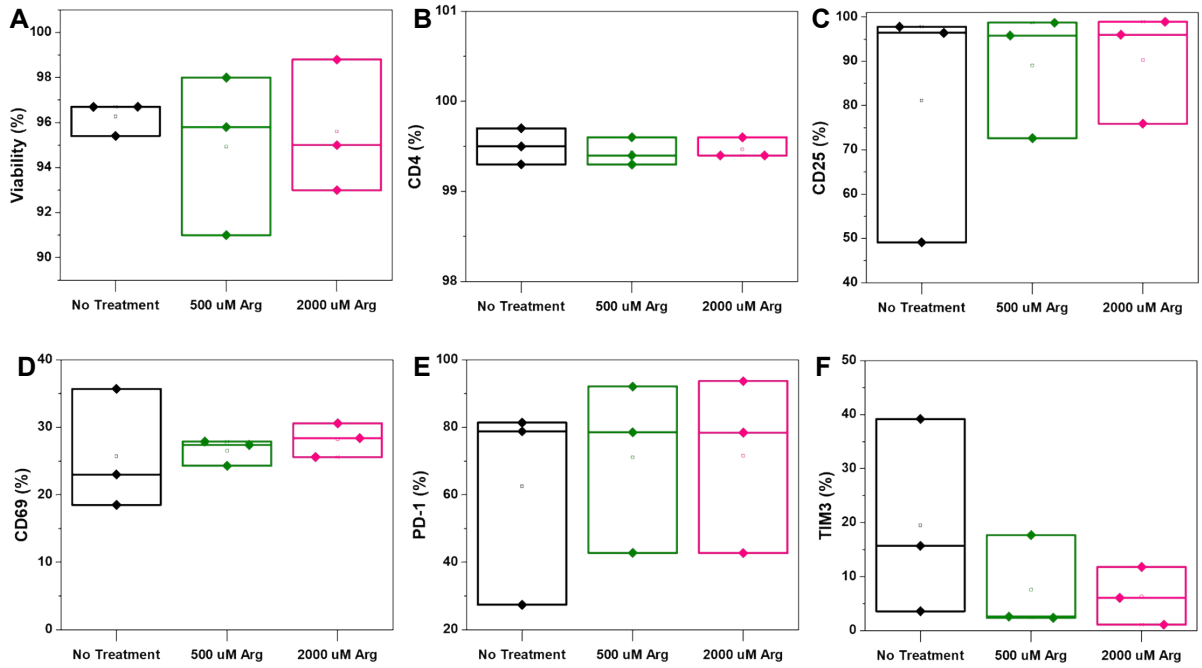

Fig. S10. Flow cytometry analysis of viability **(A)**, CD4 **(B)**, CD25 **(C)**, CD69 **(D)**, PD-1 **(E)** and TIM-3 expression **(F)** in T cells after 72 h treatment with L-Arg. Data are shown for three independent biological donors (n = 3). Each plotted point represents one donor with three technical replicates. Statistical analysis was performed using the Friedman test for repeated measures, with paired comparisons to untreated control shown as exploratory analyses.

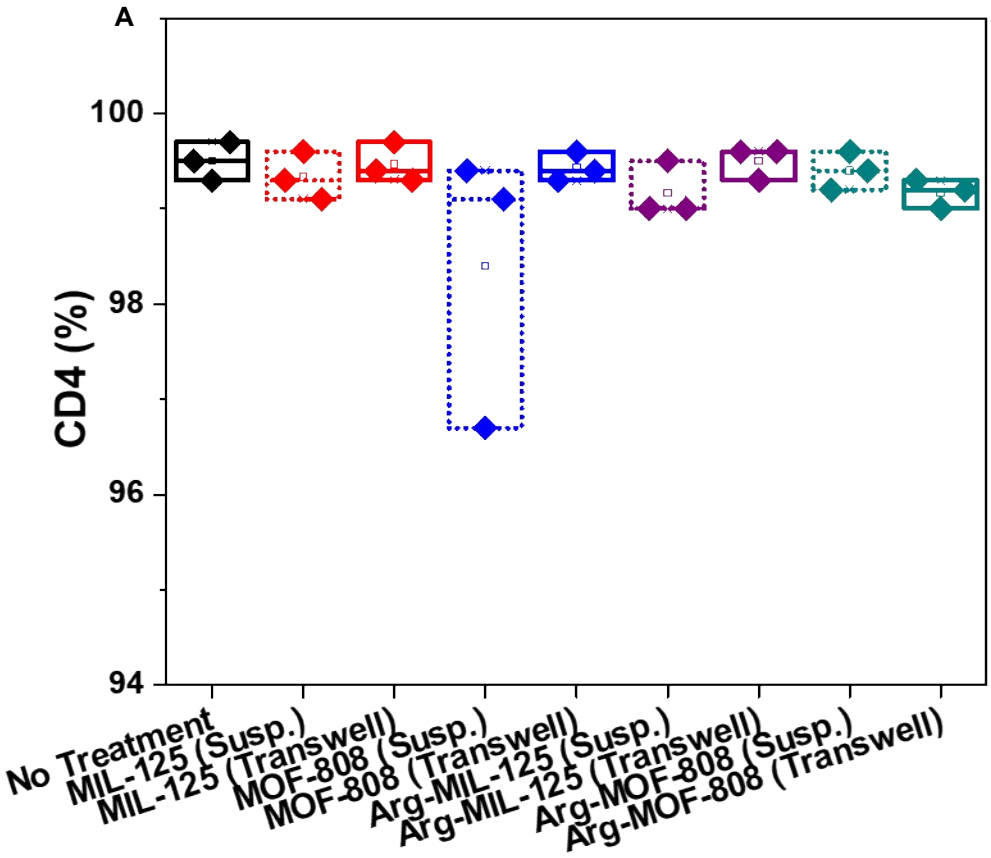
A
CD4 (%)
100
98
96
94
No Treatment
MIL-125 (Susp.)
MIL-125 (Transwell)
MOF-808 (Susp.)
MOF-808 (Transwell)
Arg-MIL-125 (Susp.)
Arg-MIL-125 (Transwell)
Arg-MOF-808 (Susp.)
Arg-MOF-808 (Transwell)

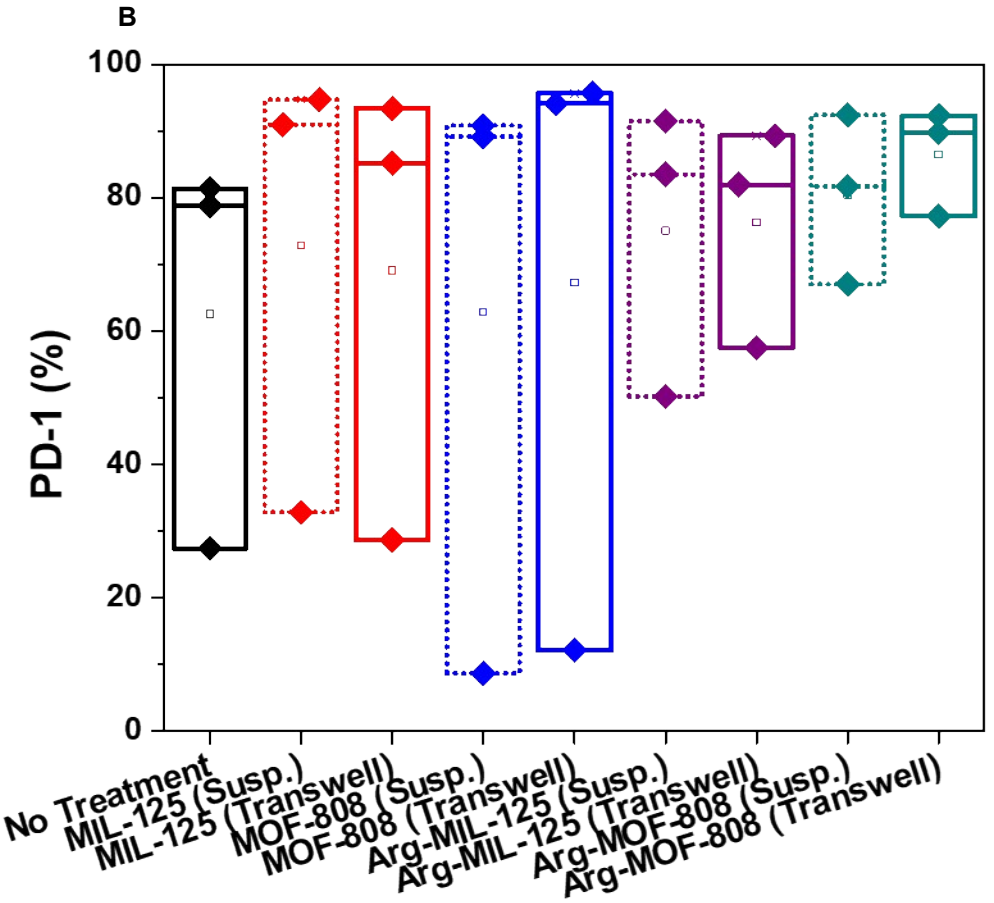
B
PD-1 (%)
100
80
60
40
20
0
No Treatment
MIL-125 (Susp.)
MIL-125 (Transwell)
MOF-808 (Susp.)
MOF-808 (Transwell)
Arg-MIL-125 (Susp.)
Arg-MIL-125 (Transwell)
Arg-MOF-808 (Susp.)
Arg-MOF-808 (Transwell)

Fig. S11. Supplementary analysis of checkpoint marker PD-1 and CD4 Markers in T cells after 72 h treatment with unloaded or Arg-loaded MOFs mixed with cells (Susp.) or seeded to transwells. Data are shown for three independent biological donors (n = 3). Each plotted point represents one donor with three technical replicates. Statistical analysis was performed using the Friedman test for repeated measures, with paired comparisons to untreated control shown as exploratory analyses.

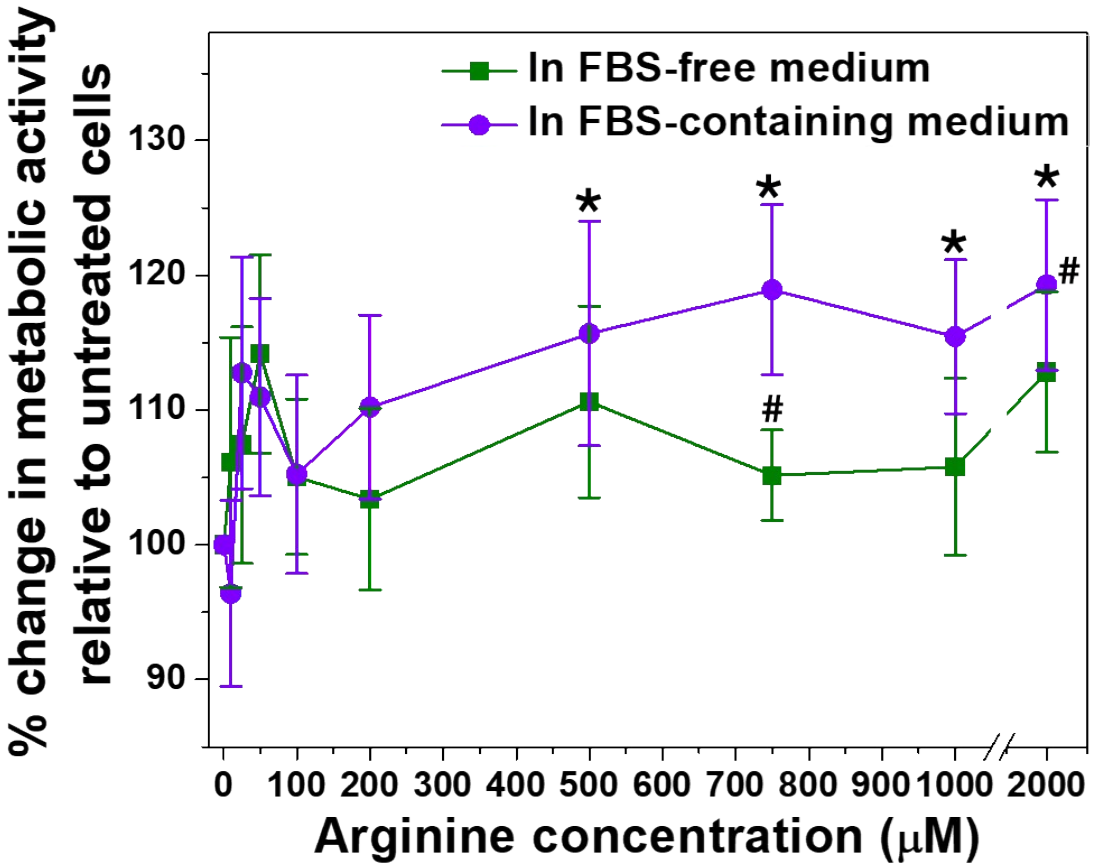

Fig. S12. Effects of arginine on the metabolic activity of iNOS-expressing MDA-MB-231 cells in both FBS-free and FBS-containing media. Data are presented as mean ± SD (n = 3). Statistical analysis was performed using two-tailed unpaired Student's t-test: $^{*}p < 0.05$ versus untreated cells in FBS- containing medium; $^{\#}p < 0.05$ versus untreated cells in FBS-free medium.

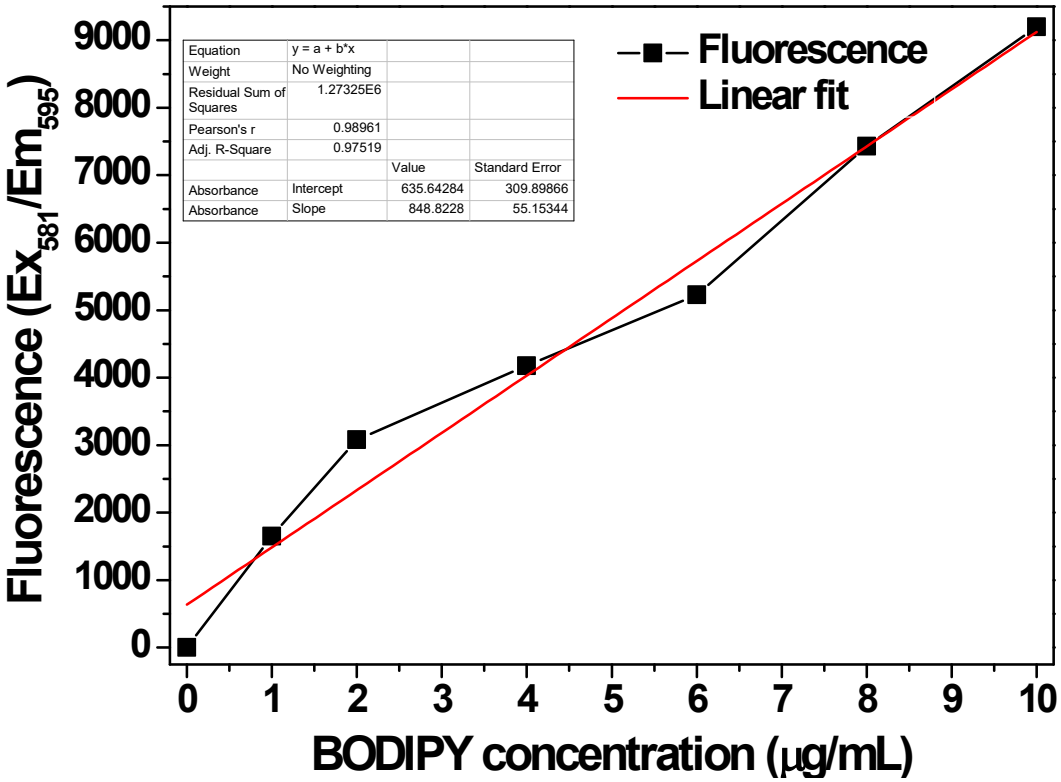

Fig. S13. Standard fluorescence calibration curve of BODIPY™ 581/591 C11 (λ_{ex} = 581 nm, λ_{em} = 595 nm).

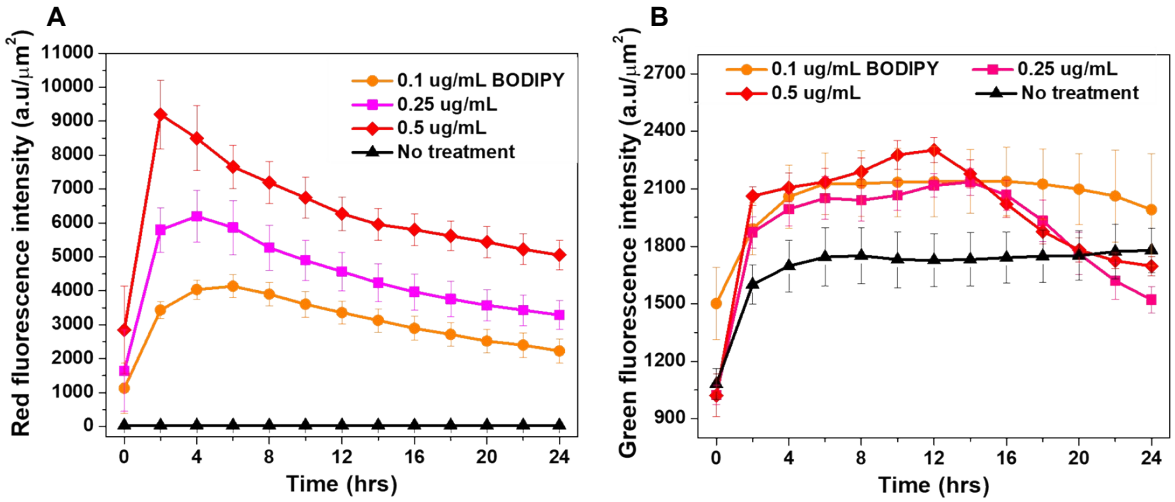

Fig. S14. Time-resolved red **(A)** and green fluorescence **(B)** in iNOS-transduced MDA-MB-231 cells treated with BODIPY™ 581/591 C11 (no carrier) in FBS-free medium.

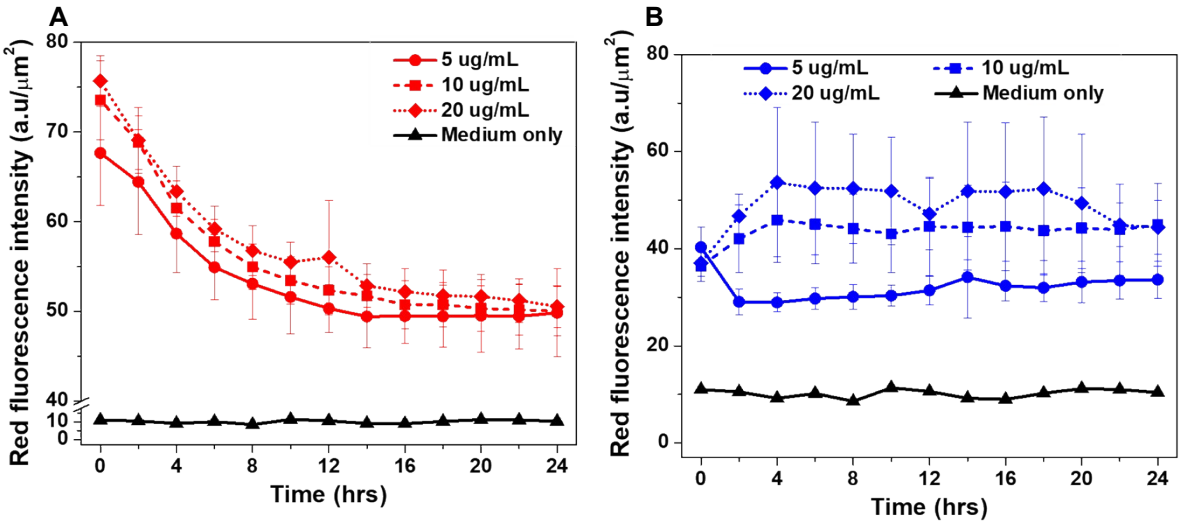

Fig. S15. Time-resolved red fluorescence in iNOS-transduced MDA-MB-231 cells treated with BODIPY™ 581/591 C11-labelled NH_2-MIL-125 **(A)** and MOF-808 nanoparticles **(B)** in FBS-free medium. Data are presented as mean ± SD (n = 3).

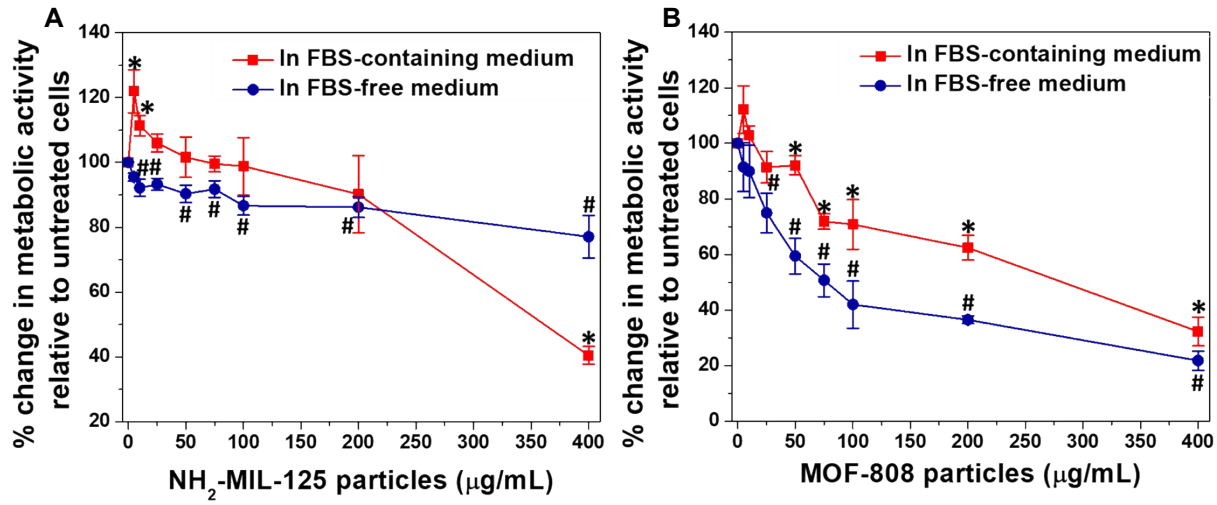

Fig. S16. Effect of NH_2-MIL-125 (a) and MOF-808 nanoparticles (b) on the metabolic activity of iNOS-expressing MDA-MB-231 cells in both FBS-free and FBS-containing media. Data are presented as mean ± SD (n = 3). Statistical analysis was performed using two-tailed unpaired Student's t-test: $^{*}p < 0.05$ versus untreated cells in FBS- containing medium; $^{\#}p < 0.05$ versus untreated cells in FBS-free medium.

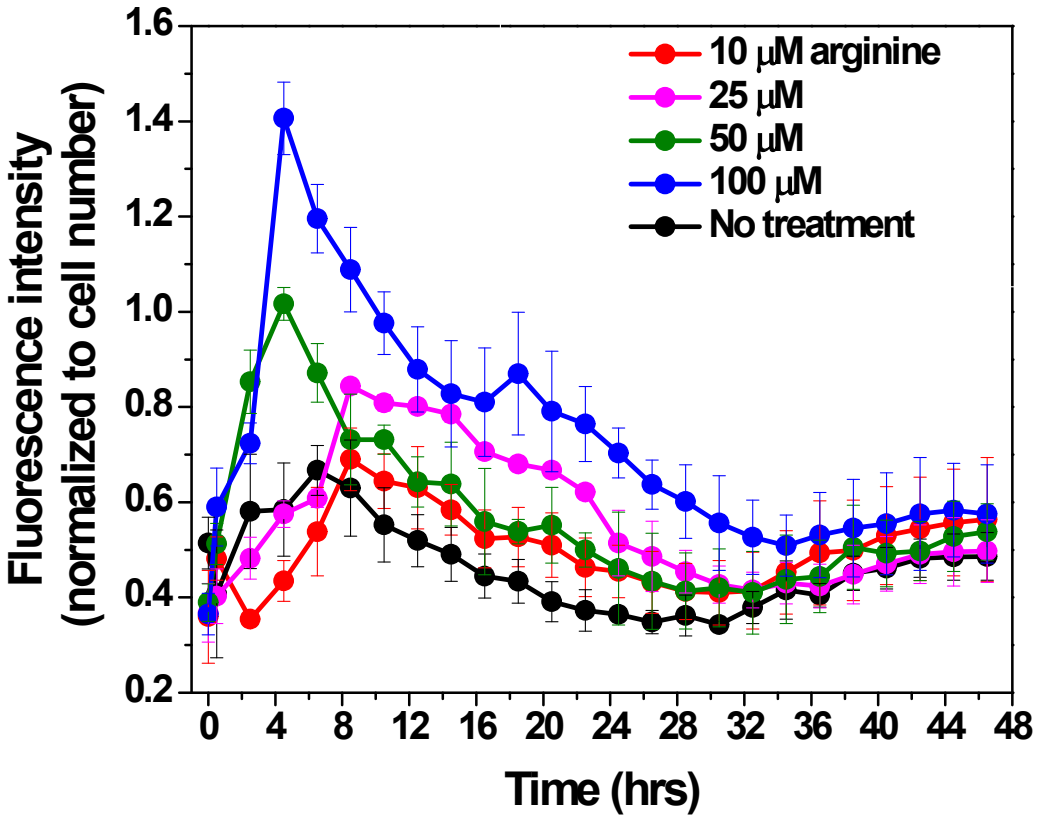

Fig. S17. Time course of intracellular •NO production in arginine-treated iNOS-transduced MDA-MB-231 cells. Data are presented as mean ± SD of the normalized fluorescence intensities (n = 4).

Insert Video S1 here

Video S1. Dual-channel live-cell fluorescence imaging showing predominant BODIPY™ 581/591 C11 (0.1 μg/mL) red signal in iNOS-transduced MDA-MB-231 cells.

Insert Video S2 here

Video S2. Dual-channel live-cell fluorescence imaging showing predominant BODIPY™ 581/591 C11 (0.25 μg/mL) red signal in iNOS-transduced MDA-MB-231 cells.

Insert Video S3 here

Video S3. Dual-channel live-cell fluorescence imaging showing predominant BODIPY™ 581/591 C11 (0.5 μg/mL) red signal in iNOS-transduced MDA-MB-231 cells.

Insert Video S4 here

Video S4. Dual-channel live-cell fluorescence imaging of iNOS-transduced MDA-MB-231 cells.

Insert Video S5 here

Video S5. Dual-channel live fluorescence imaging of BODIPY™ 581/591 C11–labelled NH_2-MIL-125 nanoparticles (5 μg/mL) in the Absence of Cells.

Insert Video S6 here

Video S6. Dual-channel live fluorescence imaging of BODIPY™ 581/591 C11–labelled NH_2-MIL-125 nanoparticles (10 μg/mL) in the Absence of Cells.

Insert Video S7 here

Video S7. Dual-channel live fluorescence imaging of BODIPY™ 581/591 C11–labelled NH_2-MIL-125 nanoparticles (20 μg/mL) in the Absence of Cells.

Insert Video S8 here

Video S8. Dual-channel live fluorescence imaging of BODIPY™ 581/591 C11–labelled MOF-808 nanoparticles (5 μg/mL) in the Absence of Cells.

Insert Video S9 here

Video S9. Dual-channel live fluorescence imaging of BODIPY™ 581/591 C11–labelled MOF-808 nanoparticles (10 μg/mL) in the Absence of Cells.

Insert Video S10 here

Video S10. Dual-channel live fluorescence imaging of BODIPY™ 581/591 C11–labelled MOF-808 nanoparticles (20 μg/mL) in the Absence of Cells.

Insert Video S11 here

Video S11. Dual-channel live-cell fluorescence imaging of iNOS-transduced MDA-MB-231 cells treated with BODIPY™ 581/591 C11–labelled NH_2-MIL-125 nanoparticles (5 μg/mL).

.

Insert Video S12 here

Video S12. Dual-channel live-cell fluorescence imaging of iNOS-transduced MDA-MB-231 cells treated with BODIPY™ 581/591 C11–labelled NH_2-MIL-125 nanoparticles (10 μg/mL).

Insert Video S13 here

Video S13. Dual-channel live-cell fluorescence imaging of iNOS-transduced MDA-MB-231 cells treated with BODIPY™ 581/591 C11–labelled NH_2-MIL-125 nanoparticles (20 μg/mL).

Insert Video S14 here

Video S14. Dual-channel live-cell fluorescence imaging of iNOS-transduced MDA-MB-231 cells treated with BODIPY™ 581/591 C11–labelled MOF-808 nanoparticles (5 μg/mL).

Insert Video S15 here

Video S15. Dual-channel live-cell fluorescence imaging of iNOS-transduced MDA-MB-231 cells treated with BODIPY™ 581/591 C11–labelled MOF-808 nanoparticles (10 μg/mL).

Insert Video S16 here

Video S16. Dual-channel live-cell fluorescence imaging of iNOS-transduced MDA-MB-231 cells treated with BODIPY™ 581/591 C11–labelled MOF-808 nanoparticles (20 μg/mL).

Insert Video S17 here

Video S17. Real-time monitoring of •NO release kinetics in live iNOS-transduced MDA-MB-231 cells treated with dispersed NH_2-MIL-125 nanoparticles.

Insert Video S18 here

Video S18. Real-time monitoring of •NO release kinetics in live iNOS-transduced MDA-MB-231 cells treated with dispersed arginine-loaded NH_2-MIL-125 nanoparticles.

Insert Video S19 here

Video S19. Real-time monitoring of •NO release kinetics in live iNOS-transduced MDA-MB-231 cells treated with sonicated NH_2-MIL-125 nanoparticles.

Insert Video S20 here

Video S20. Real-time monitoring of •NO release kinetics in live iNOS-transduced MDA-MB-231 cells treated with sonicated arginine-loaded NH_2-MIL-125 nanoparticles.

Insert Video S21 here

Video S21. Real-time monitoring of •NO release kinetics in live iNOS-transduced MDA-MB-231 cells treated with dispersed MOF-808 nanoparticles.

Insert Video S22 here

Video S22. Real-time monitoring of •NO release kinetics in live iNOS-transduced MDA-MB-231 cells treated with dispersed arginine-loaded MOF-808 nanoparticles.

Insert Video S23 here

Video S23. Real-time monitoring of •NO release kinetics in live iNOS-transduced MDA-MB-231 cells treated with sonicated MOF-808 nanoparticles.

Insert Video S24 here

Video S24. Real-time monitoring of •NO release kinetics in live iNOS-transduced MDA-MB-231 cells treated with sonicated arginine-loaded MOF-808 nanoparticles.

Insert Video S25 here

Video S25. Real-time monitoring of •NO release kinetics in live untreated iNOS-transduced MDA-MB-231 cells.

Insert Video S26 here

Video S26. Time-lapse scratch assay showing wound closure in untreated iNOS-transduced MDA-MB-231 cells.

Insert Video S27 here

Video S27. Time-lapse scratch assay showing wound closure in iNOS-transduced MDA-MB-231 cells treated with sonicated NH_2-MIL-125 nanoparticles.

Insert Video S28 here

Video S28. Time-lapse scratch assay showing wound closure in iNOS-transduced MDA-MB-231 cells treated with sonicated arginine-loaded NH_2-MIL-125 nanoparticles.

Insert Video S29 here

Video S29. Time-lapse scratch assay showing wound closure in iNOS-transduced MDA-MB-231 cells treated with sonicated MOF-808 nanoparticles.

Insert Video S30 here

Video S30. Time-lapse scratch assay showing wound closure in iNOS-transduced MDA-MB-231 cells treated with sonicated arginine-loaded MOF-808 nanoparticles.

References

1. J. Y. Oh, E. Choi, B. Jana, E. M. Go, E. Jin, S. Jin, J. Lee *et al.*, *Small*, 2023, **19**.
2. J. M. Peula and F. J. de las Nieves, *Colloids Surf. A Physicochem. Eng. Asp.*, 1994, **90**, 55–62.

3. S. Vilela, P. Salcedo-Abraira, I. Colinet, F. Salles, M. De Koning, M. Joosen, C. Serre and P. Horcajada, *Nanomaterials*, 2017, **7**, 321.
4. N. J. Castellanos, Z. M. Rojas, H. A. Camargo, S. Biswas and G. Granados-Oliveros, *Transition Met. Chem.*, 2019, **44**, 77–87.
5. Y.-S. Lin, K.-S. Lin, N. V. Mdlovu, M.-T. Weng, W.-C. Tsai and U.-S. Jeng, *Biomater. Adv.*, 2022, **140**, 213070.
6. Y. Zhao, W. Cai, J. Chen, Y. Miao and Y. Bu, *Front. Chem.*, 2019, **7**.
7. H. Embrechts, M. Kriesten, M. Ermer, W. Peukert, M. Hartmann and M. Distaso, *RSC Adv.*, 2020, **10**, 7336–7348.
8. R. J. Hunter, *Zeta Potential in Colloid Science: Principles and Applications*, Academic Press, 2014.
9. E. Bellido, M. Guillevic, T. Hidalgo, M. J. Santander-Ortega, C. Serre and P. Horcajada, *Langmuir*, 2014, **30**, 5911–5920.
10. C. Jia, F. G. Cirujano, B. Bueken, B. Claes, D. Jonckheere, K. M. Van Geem and D. De Vos, *ChemSusChem*, 2019, **12**, 1256–1266.
11. K. D. Nguyen, N. T. Vo, K. T. M. Le, K. V. Ho, N. T. S. Phan, P. H. Ho and H. V. Le, *New J. Chem.*, 2023, **47**, 6433–6447.
12. I. Romero-Muñiz, C. Romero-Muñiz, I. del Castillo-Velilla, C. Marini, S. Calero, F. Zamora and A. E. Platero-Prats, *ACS Appl. Mater. Interfaces*, 2022, **14**, 27040–27047.
13. J. A. Mancillas-Quiroz, M. del C. Carrasco-Portugal, K. Mondragón-Vásquez, J. C. Huerta-Cruz, J. Rodríguez-Silverio, L. Rodríguez-Vera, J. G. Reyes-García *et al.*, *Pharmaceutics*, 2024, **17**, 11.
14. S. Kumar and S. B. Rai, *Indian J. Pure Appl. Phys.*, 2010, **48**, 251–255.
15. M. Dan-Hardi, C. Serre, T. Frot, L. Rozes, G. Maurin, C. Sanchez and G. Férey, *J. Am. Chem. Soc.*, 2009, **131**, 10857–10859.
16. G. Férey, *Chem. Soc. Rev.*, 2008, **37**, 191–214.
17. N. Stock and S. Biswas, *Chem. Rev.*, 2012, **112**, 933–969.
18. P. Horcajada, R. Gref, T. Baati, P. K. Allan, G. Maurin, P. Couvreur, G. Férey, R. E. Morris and C. Serre, *Chem. Rev.*, 2012, **112**, 1232–1268.